

Broadband type-I hyperbolicity independent of carrier density in RuOCl₂ crystals

Han Gao^{1,2,*}, Xuejin Zhang^{2,*}, Mingzheng Wang², Chao Ding², Ning Qu¹, Bo Yang¹ and Mingwen Zhao^{2,‡}

¹*School of Science, Shandong Jianzhu University, Jinan 250100, China*

²*School of Physics, Shandong University, Jinan 250100, Shandong, China*

 (Received 7 November 2023; revised 9 March 2024; accepted 12 March 2024; published 25 March 2024)

The design and fabrication of hyperbolic metamaterials require precise control over the arrangement and dimensions of constituent components, such as nanosheets or nanowires, to achieve the desired hyperbolic dispersion. However, the ongoing challenge lies in further downsizing these components to broaden the hyperbolic regime and enhance the maximal wave vector. In this study, we propose a linear quasi-one-dimensional electron gas array model as a promising category of type-I natural hyperbolic materials (NHMs). The hyperbolic properties in these NHMs remain insensitive to the position of the Fermi level, owing to the linear dispersion relation near the Fermi level. Through first-principles calculations, we have identified a highly promising candidate material, the RuOCl₂ crystal, for this model. Our research demonstrates that the RuOCl₂ crystal exhibits a broad type-I hyperbolic region that spans from the infrared to the entire visible spectrum, and this property is nearly independent of the Fermi level's position, or equivalently, the carrier density. We also investigate the exceptional negative refraction effects and directional-propagating surface plasmon polaritons that arises from the hyperbolic equifrequency contour. These findings offer a universal approach to designing type-I NHMs, as well as a compelling foundation for development of cutting-edge optoelectronic devices.

DOI: [10.1103/PhysRevB.109.115432](https://doi.org/10.1103/PhysRevB.109.115432)

I. INTRODUCTION

The dielectric properties of a nonmagnetic bulk material can be characterized using a permittivity tensor

$$\hat{\epsilon} = \begin{pmatrix} \epsilon_{xx} & 0 & 0 \\ 0 & \epsilon_{yy} & 0 \\ 0 & 0 & \epsilon_{zz} \end{pmatrix}. \quad (1)$$

For a uniaxial material, supposing the permittivity tensor exhibits isotropy in the x - z plane, $\epsilon_{xx} = \epsilon_{zz} \equiv \epsilon_{\perp}$, $\epsilon_{yy} \equiv \epsilon_{//}$, the equifrequency contour (EFC) for transverse magnetic (TM) polarized electromagnetic waves (k_x , k_y) of light incident along the anisotropy axis (y axis) is given by the expression [1]

$$\frac{k_x^2}{\epsilon_{//}} + \frac{k_y^2}{\epsilon_{\perp}} = \frac{\omega^2}{c^2}. \quad (2)$$

The shape of the EFC, whether it resembles an ellipse or a hyperbola, is contingent upon the signs of the two permittivity tensor components. In the context of normal anisotropic materials, the tensor components lead to an elliptical EFC as $\epsilon_{\perp} > 0$, $\epsilon_{//} > 0$, and $\epsilon_{\perp} \neq \epsilon_{//}$. Conversely, when $\epsilon_{//} \times \epsilon_{\perp} < 0$, the EFC assumes a hyperbolic form, and this class of materials is recognized as hyperbolic materials (HMs), which can be further categorized into two distinct types: type-I ($\epsilon_{//} > 0$ & $\epsilon_{\perp} < 0$) and type-II ($\epsilon_{//} < 0$ & $\epsilon_{\perp} > 0$) [2,3]. The distinctive hyperbolicity of the EFC within the wavevector

space unlocks a multitude of promising applications for HMs, such as all-angle negative refraction [4,5], subwavelength imaging in the far-field [6], and enhancement of spontaneous emission [7,8], which have been achieved within the realm of metamaterials.

Hyperbolic metamaterials (HMMs) are a fascinating class of artificially engineered materials that exhibit exotic optical properties, often characterized by hyperbolic dispersion relations [9]. HMMs have garnered significant attention in the fields of photonics, optics, and nanotechnology due to their unique ability to manipulate and control the flow of light [10,11]. The design and fabrication of HMMs require precise control over the arrangement and dimensions of constituent elements, such as nanosheets or nanowires, to achieve the desired hyperbolic dispersion. However, fabricating such materials with the desired properties across a wide range of wavelengths and suppressing the energy loss due to interface scattering remain a challenging task.

The emergency of natural hyperbolic materials (NHMs) offers a promising avenue for overcoming the limitations associated with HMMs, owing to their low-loss properties, broadband electromagnetic response and higher light confinement [12–15]. These appealing characteristics render NHMs highly attractive for a wide range of optical and photonics applications [16,17].

Certain layered van der Waals (vdW) materials, including graphite [18] and transition metal dichalcogenides (TMDs) [19], have been identified as NHMs, due to their inherent anisotropy between in-plane and out-of-plane directions. Specifically, the in-plane orientation typically exhibits a stronger metallic behavior compared to the out-of-plane direction, reminiscent of hyperbolic metamaterials (HMMs)

*These authors contributed equally to this work.

†Corresponding author: gaohan22@sdjzu.edu.cn

‡Corresponding author: zmw@sdu.edu.cn

created by incorporating metallic sheets within dielectric media. This features render layered vdW materials well suited for type-II hyperbolic materials rather than type-I ones [20].

Additionally, the negative component of the permittivity tensor, which is determined by the long-wavelength plasmon frequency (ω_p), strongly depends on the carrier density (n) in these NHMs. For example, in conventional three-dimensional (3D) metals, the plasmon frequency is proportional to $n^{1/2}$, while in 3D massless Dirac systems, it scales with $n^{1/3}$ [21–24]. This sensitivity on n implies that the shape of the EFC in these materials can be manipulated by fine-tuning the carrier density through methods like chemical doping and gating at specific wavelengths, granting precise control over the propagation behavior of electromagnetic waves. However, it is worth noting that this dependence on carrier density also makes the hyperbolic response susceptible to disturbances from the surrounding environment, rendering it vulnerable to instability when subjected to defects, thermal perturbations, and other factors that significantly affect the carrier density [25–28]. Recently, anomalous n independence has been observed in 3D topological semimetals with nodal surfaces [29]. Nonetheless, the relatively weak anisotropy and the emergence of electron-hole pairs due to the crossing of conduction and valence bands near the Fermi level on closed nodal surfaces make this class of systems unsuitable as NHMs [30].

In this study, we propose a linear quasi-one-dimensional electron gas array (Q1DEGA) model for type-I NHMs. This model harnesses the intrinsic inherent electronic anisotropy arising from its unidirectional electron conducting nature, providing a broad spectral hyperbolic response, characterized by type-I hyperbolicity. Crucially, the long-wavelength plasmon frequency ω_p exhibits a remarkable property of independence from carrier density (n), thereby conferring stable hyperbolicity that remains resilient to external disturbances from the surrounding environment affecting the carrier density. Through first-principles calculations, we identified a promising material, the already-synthesized RuOCl_2 [31], for this model. Our calculations demonstrated that the RuOCl_2 crystal exhibits highly anisotropic electronic structure along with a broad band type-I hyperbolic region spanning from 369 nm to 15.5 μm . This hyperbolic region covers from the infrared to the entire visible spectrum region with low optical loss. Furthermore, both the long-wavelength plasmon frequency and hyperbolic interval of RuOCl_2 are nearly independent of electron doping concentration. Our numerical simulations based on Maxwell's equations also manifest exotic all-angle negative refraction of transverse magnetic (TM) waves and hyperbolic surface plasmon polaritons (SPPs) on the (001) surface of RuOCl_2 resulting from the hyperbolic EFC. These results not only present an innovative approach to designing type-I NHMs but also introduce RuOCl_2 as a promising NHM candidate, offering a compelling foundation for the development of cutting-edge optoelectronic devices.

II. METHOD AND COMPUTATIONAL DETAILS

Our first-principles calculations were performed using density functional theory (DFT), as implemented in the Vienna *ab initio* simulation package (VASP) [32]. The projected augmented-wave method was employed to model

interactions between electrons and ions [33]. The exchange-correlation functional was treated self-consistently within the generalized gradient approximation (GGA) using the Perdew-Burke-Ernzerhof (PBE) functional [34]. The cutoff energy for the plane wave basis was set to 500 eV. Structure relaxation and electronic properties were calculated using VASP with the Γ (0,0,0)-centered k -point mesh of $11 \times 11 \times 11$ and $14 \times 14 \times 4$ for primitive cell and conventional cell of bulk RuOCl_2 , respectively. The settings of the cutoff energy and k -point mesh were tested to ensure the energy converged to 0.001 eV/atom. The van der Waals (vdW) interaction was considered by using the DFT-D3 strategy [35]. The GGA + U method [36] accounting for strong Coulomb interaction between the partially filled $4d$ shells of Ru was also employed with the effective Hubbard interaction parameter of $U_{\text{eff}} = 2$ eV (where $U = 2$ eV and $J = 0$ eV), as implemented in previous works on Ru compounds [37–39]. The lattice constants and the atomic positions were fully relaxed until the atomic forces on the atoms were less than 0.01 eV/Å and the total energy change was less than 10^{-5} eV. The numerical simulations of negative refraction and propagation of surface waves were carried out in a $6 \mu\text{m} \times 6 \mu\text{m}$ RuOCl_2 sample, using the finite-element method (FEM) implemented in COMSOL MULTIPHYSICS [40].

III. RESULTS AND DISCUSSION

A. Quasi-one-dimensional electron gas array model

The Q1DEGA model introduced in our study describes a 3D system in which the electron moment is strictly confined to a single direction, specifically along the y axis, while it is categorically restricted along the other two axes (x and z axes). This distinctive trait is manifested in the electronic structure, which exhibits a planar Fermi surface orthogonal to the y direction, as depicted in the left panel of Fig. 1(a). We consider a special case characterized by a linear energy-momentum dispersion along the y direction, $E(k) = v_F k_y$, irrespective of k_x and k_z , as depicted in the right panel of Fig. 1(a). This distinctive dispersion relation represents highly anisotropic electronic structures along the out-of-plane (k_y) and in-plane (k_x and k_z) directions. Consequently, these structures are expected to induce significant optical anisotropy and enhanced anisotropic interaction between light and matter [41].

The permittivity tensor components, $\varepsilon_{jj}(\omega)$, $j = x, y, z$, of the Q1DEGA system can be expressed in a simplified form as follows [42]:

$$\varepsilon_{jj}(\omega) = 1 - \frac{\omega_{p,j}^2}{\omega^2 + i\eta\omega} - \frac{\Omega_j^2}{\omega^2 - \omega_{0,j}^2 + i\gamma\omega} + \varepsilon_r. \quad (3)$$

In this expression, $\omega_{p,j}$ represents the long-wavelength plasmon frequency along the j direction, Ω_j accounts for the strength of the interband component, $\omega_{0,j}$ is the onset frequency of the interband transitions, and η and γ denote the lifetime broadening of intraband and interband transitions, respectively. The second and third terms signify contributions of intraband and interband transitions of electrons. The last term ε_r encapsulates the contributions of other factors, including

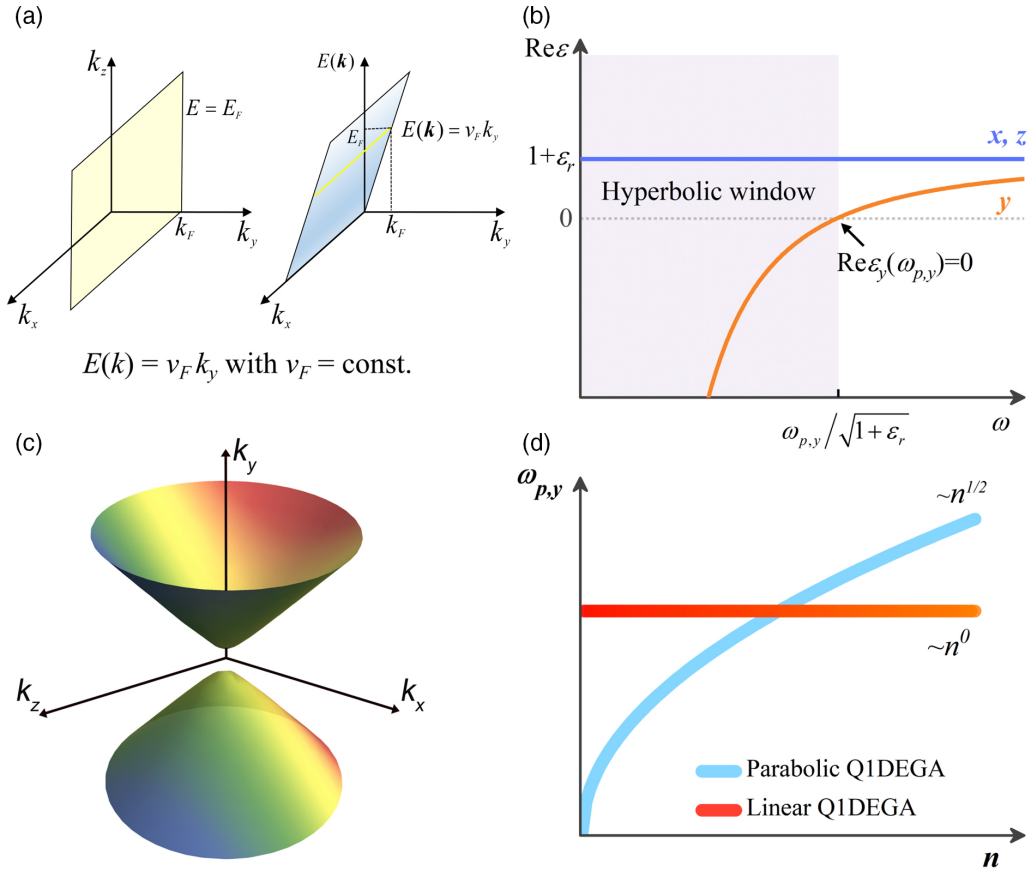


FIG. 1. Schematic representation of Q1DEGA model. (a) Left: Schematic plot of the Fermi surface for Q1DEGA system. Right: The linear dependence of energy E with k_y , where the slope v_F is a constant. (b) The real part of the permittivity for Q1DEGA systems. The shaded region stands for the hyperbolic region with $\text{Re } \epsilon_{xx} > 0$, $\text{Re } \epsilon_{zz} > 0$, $\text{Re } \epsilon_{yy} < 0$. (c) Equipfrequency contours (EFC) for Q1DEGA systems for $\omega < \omega_{p,y}$. (d) Dependencies of plasmon frequency on the carrier density in the long-wavelength limit for parabolic and linear Q1DEGA systems.

the dielectric background and those beyond the scope of the Q1DEGA model.

Within the random phase approximation (RPA), the dynamic dielectric function $\epsilon(\mathbf{q}, \omega)$ is determined from the polarization function using the equation [21]

$$\epsilon(\mathbf{q}, \omega) = 1 - V(\mathbf{q})\Pi(\mathbf{q}, \omega). \quad (4)$$

In this expression, the Fourier transform of Coulomb potential $V(\mathbf{q})$ should take a 3D form, $V(\mathbf{q}) = 4\pi e^2/q^2$, because the Q1DEGA model proposed in this study is grounded in a 3D system. Plasmon dispersion is determined by the zeros of the dielectric function $\epsilon(\mathbf{q}, \omega)$. Assuming the intraband transitions of electrons dominate the dielectric function, the polarization function $\Pi(\mathbf{q}, \omega)$ can be written in the Lindhard expression [21],

$$\Pi(\mathbf{q}, \omega) = \frac{g}{(2\pi)^3} \int d^3k \frac{f(E_k) - f(E_{k+q})}{\omega + E_k - E_{k+q} + i\eta}. \quad (5)$$

Here g is the generator factor and $f(E)$ is the Fermi distribution function. In the long wavelength approximation ($q \rightarrow 0$), the polarization function of the Q1DEGA model can be expressed in a simplified form as [43]

$$\Pi(\mathbf{q} \rightarrow 0, \omega) \approx \frac{gSv_F}{4\pi^3\omega^2} q^2 \cos^2\theta_q, \quad (6)$$

where S is the projected area of the Brillouin zone on the k_x-k_z plane and θ_q represents the angle between \mathbf{q} and k_y . The plasmon frequency of the Q1DEGA model in the long-wavelength limit is reduced to

$$\omega_p(\mathbf{q} \rightarrow 0) \approx \sqrt{ge^2v_FS|\cos\theta_q|/\pi^2}. \quad (7)$$

Obviously, we got anisotropic plasmon frequencies along the x , y , and z directions at $q = 0$, which are $\omega_{p,x} \approx \omega_{p,z} = 0$ and $\omega_{p,y} \approx \sqrt{ge^2v_FS/\pi^2}$. The plasmon frequencies are independent of the position of Fermi level (or equivalently electron density), in contrast to the normal 3D metals.

From the anisotropic plasmon frequencies, one can readily access the hyperbolic region within the framework of the Q1DEGA model, according to Eq. (3). For simplification, we have omitted the imaginary part of the permittivity. The permittivity tensor components can be expressed as $\epsilon_{xx}(\omega) = \epsilon_{zz}(\omega) \equiv \epsilon_{//} = 1 + \epsilon_r$ and $\epsilon_{yy}(\omega) \equiv \epsilon_{\perp}(\omega) = 1 - \omega_{p,y}^2/\omega^2 - \Omega_y^2/(\omega^2 - \omega_0^2) + \epsilon_r$. If both Ω_y and ϵ_r are insensitive to the position of Fermi level, as observed in the case of $\omega_{p,y}$, the components of permittivity tensor become independent of the position of Fermi level (or equivalently carrier density). Specifically, neglecting the contribution from interband transitions, e.g., in the case of $\omega \ll \omega_0$, results in a type-I hyperbolic region of $0 < \omega < \omega_{p,y}/\sqrt{1 + \epsilon_r}$. It is

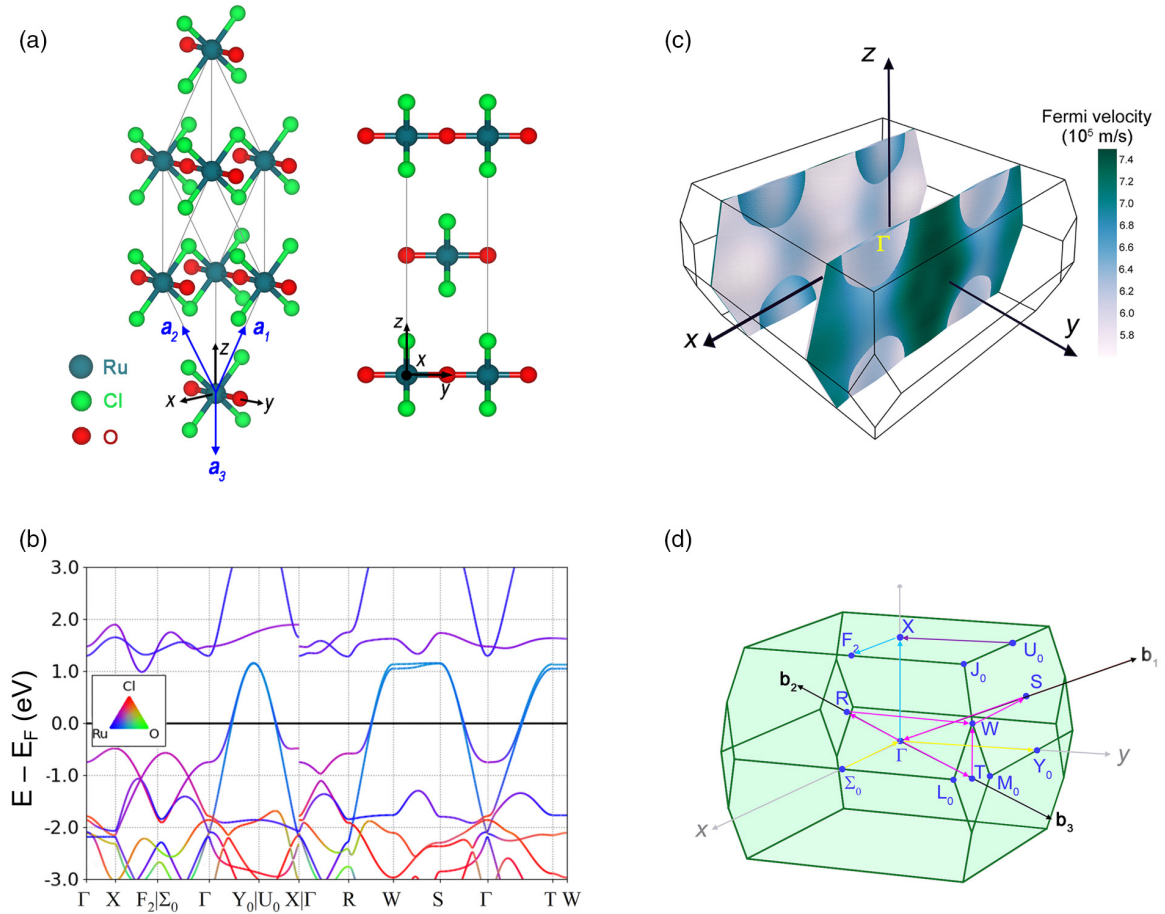


FIG. 2. Lattice and electronic structures of bulk RuOCl₂ crystal. (a) Schematic views of the primitive cell (left panel) and conventional cell (right panel) of bulk RuOCl₂. (b) Atom-resolved electronic band structure of bulk RuOCl₂. (c) Fermi surface of bulk RuOCl₂, with the color representing the magnitude of the Fermi velocity. (d) Schematic diagram of the Brillouin zone and the high symmetry points of bulk RuOCl₂.

noteworthy that this characteristic is intricately linked to the distinct linear dispersion relation inherent to the Q1DEGA model. In contrast, for a parabolic dispersion relation, $E(k) = k_y^2/2m_e^*$, the plasmon frequency $\omega_{p,y}$ scales proportionally with $n^{1/2}$, as depicted in Fig. 1(d). The inclusion of interband transitions would introduce a dependence of the hyperbolic region on the position of Fermi level, if Ω_j exhibits dependence on the Fermi level position.

B. Hyperbolicity of RuOCl₂ crystal

We now consider an experimentally synthesized material, RuOCl₂, whose lattice structure is characterized by Ru-O arrays along the b axis, as an example to verify the aforementioned theoretical design [31]. The crystal structure of bulk RuOCl₂ has a layered configuration with the space group $Immm$. The primitive cell of RuOCl₂ possesses an orthorhombic structure, as shown in Fig. 2(a), characterized by the lattice parameters of $a_1 = a_2 = a_3 = 6.27 \text{ \AA}$ and angles of $\alpha = 146.88^\circ$, $\beta = 145.63^\circ$, and $\gamma = 48.48^\circ$ from our calculations, which are consistent with the experimental values [31]. On the other hand, the conventional cell is represented as a cuboid representation with dimensions $a = 3.57 \text{ \AA}$, $b = 3.70 \text{ \AA}$, and $c = 11.43 \text{ \AA}$. Each layer of RuOCl₂ contains three atomic sublayers with the RuO plane being sandwiched

between two Cl layers. The interactions between these layers are governed by weak vdW forces. The layered structure of RuOCl₂ introduces structural anisotropy between the in-plane (xy plane) and out-of-plane (z axis) directions. Additionally, the Ru atoms are connected by two Cl atoms along the x direction and bonded by an O atom along the y direction, leading to in-plane structural anisotropy. This anisotropic structure is significant in determining the electronic, optical, and transport properties of RuOCl₂.

The band structure of bulk RuOCl₂ is presented in Fig. 2(b), where the two bands crossing the Fermi level are primarily contributed by the Ru atoms and display significant anisotropy along the three principal directions. Along the y direction (e.g., $\Gamma-Y_0$ and U_0-X), these bands show high dispersion and a nearly linear energy-momentum ($E-k$) relationship. However, along the x direction (e.g., $\Gamma-\Sigma_0$ and $X-F_2$) and z direction ($\Gamma-X$ and $T-W$), a pseudogap is observed, indicating semiconductorlike characteristics. To provide a more visual representation of the electronic properties, the Fermi surface of bulk RuOCl₂ is depicted in Fig. 2(c). The Fermi surfaces are only distributed along the $x-z$ plane, while the Fermi velocity is predominantly oriented along the y direction. It can be observed that the electronic properties of RuOCl₂ exhibit similarities to those of the Q1DEGA model, in which the Ru-O arrays conceptually mirror the

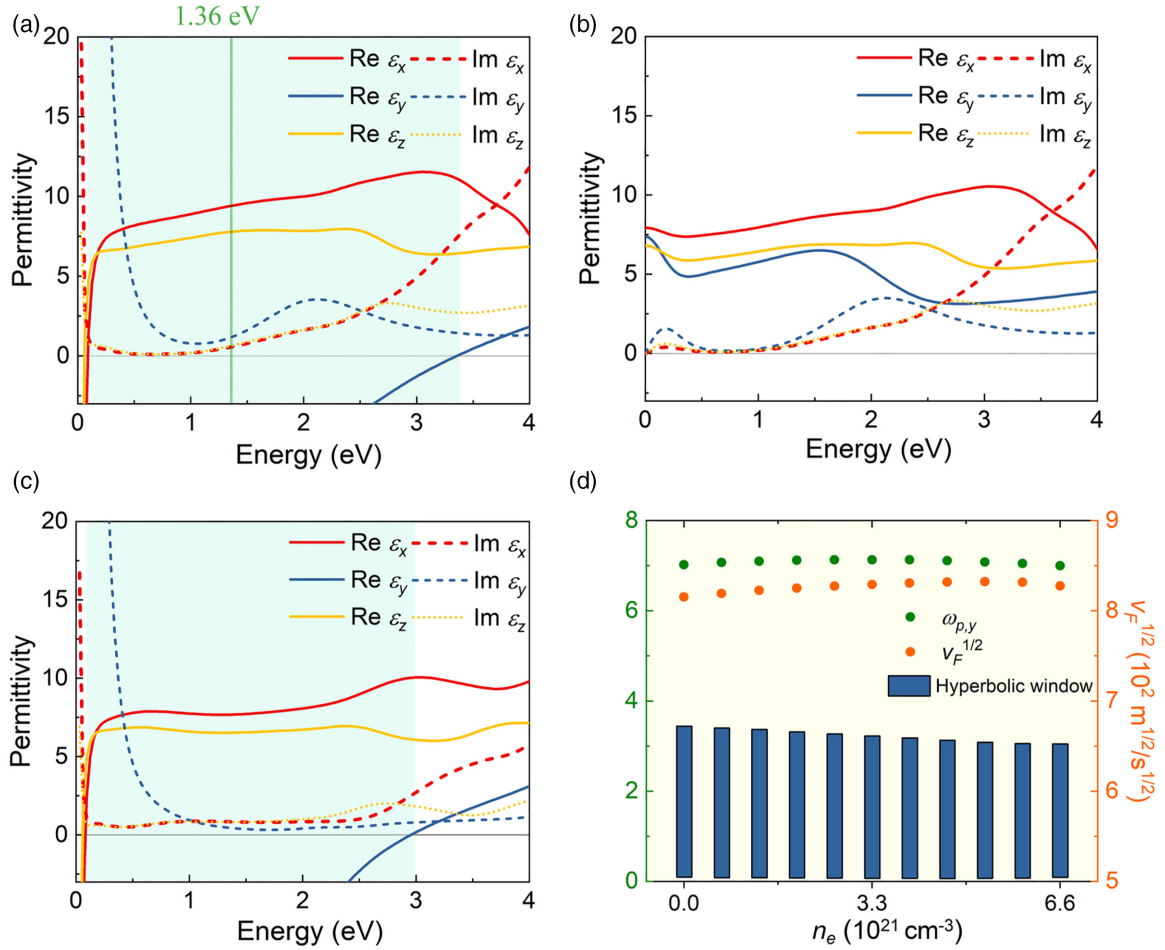


FIG. 3. Dielectric properties of bulk RuOCl₂ crystal. (a) Real and imaginary parts of the permittivity along three principal directions of pristine RuOCl₂ crystal. (b) The contributions of electron interband transitions to the real and imaginary parts of the permittivity of pristine RuOCl₂ crystal. (c) Real and imaginary parts of the permittivity along three principal directions for bulk RuOCl₂ at the electron doping concentration of $6.6 \times 10^{21} \text{ cm}^{-3}$. (d) Variation of the plasmon frequency (green dots), squared Fermi velocity (orange dots), and hyperbolic interval (dark blue bars) of bulk RuOCl₂ as a function of electron doping concentration. The shaded region in (a) and (c) shows the hyperbolic frequency window.

conducting channels depicted in Fig. 1(a). These highly anisotropic electronic properties are also anticipated to result in directional dielectric response. Remarkably, the magnitude of the Fermi velocity (v_F) along the y direction in RuOCl₂ can reach $7.4 \times 10^5 \text{ m/s}$, which is comparable to the Fermi velocity of graphene (approximately $8.5 \times 10^5 \text{ m/s}$) [44,45]. This implies that RuOCl₂ possesses a large $\omega_{p,y}$ and a broad hyperbolic window. These characteristics further support the notion that RuOCl₂ exhibits properties akin to the Q1DEGA model.

The permittivity of bulk RuOCl₂ along the three principal directions is illustrated in Fig. 3(a), revealing a highly anisotropic dielectric response. The imaginary term of the permittivity $\text{Im } \varepsilon_{jj}^{\text{inter}}$ contributed from the interband transitions was calculated using the expression

$$\text{Im } \varepsilon_{jj}^{\text{inter}} = \frac{4\pi^2 e^2}{V_c} \lim_{q \rightarrow 0} \frac{1}{q^2} \sum_{c,v,\mathbf{k}} 2w_{\mathbf{k}} \delta(E_{c\mathbf{k}} - E_{v\mathbf{k}} - \omega) \times |\langle u_{c\mathbf{k}+q} | u_{v\mathbf{k}} \rangle|^2. \quad (8)$$

Here the indices c and v are restricted to the conduction and the valence band states respectively, $u_{c\mathbf{k}}$ is the cell periodic

part of the orbitals at the \mathbf{k} , $w_{\mathbf{k}}$ represents the k -point weights and V_c is the volume of the primitive cell. The real term $\text{Re } \varepsilon_{jj}^{\text{inter}}$ is determined accordingly using the Kramers-Kronig relation [46]. For contribution from the intraband transitions, the Drude model, as expressed in the second term of Eq. (3), is used to describe transitions within the partially occupied Q1DEG bands. The lifetime broadening parameter η was fixed at 0.01 eV, and its variation has a negligible effect on the hyperbolic interval of RuOCl₂. From Fig. 3(b), one can find that the interband transitions always lead to positive $\text{Re } \varepsilon_{jj}^{\text{inter}}$ values along the three directions. This suggests that the hyperbolic response of RuOCl₂ is predominantly governed by the intraband transitions which introduce a negative permittivity component along the y direction. In the energy range 0.08–3.36 eV (369 nm–15.5 μm), bulk RuOCl₂ demonstrates characteristics of a broadband type-I hyperbolic material, meeting the conditions of $\text{Re } \varepsilon_{xx}$, $\text{Re } \varepsilon_{zz} > 0$, and $\text{Re } \varepsilon_{yy} < 0$. The low plasmon frequencies in the x and z directions, $\omega_{p,x} = 0.26 \text{ eV}$ and $\omega_{p,z} = 0.16 \text{ eV}$, result in $\text{Re } \varepsilon_x$ and $\text{Re } \varepsilon_z$ switching from negative to positive at extremely low energies. Conversely, the large plasmon frequency in the

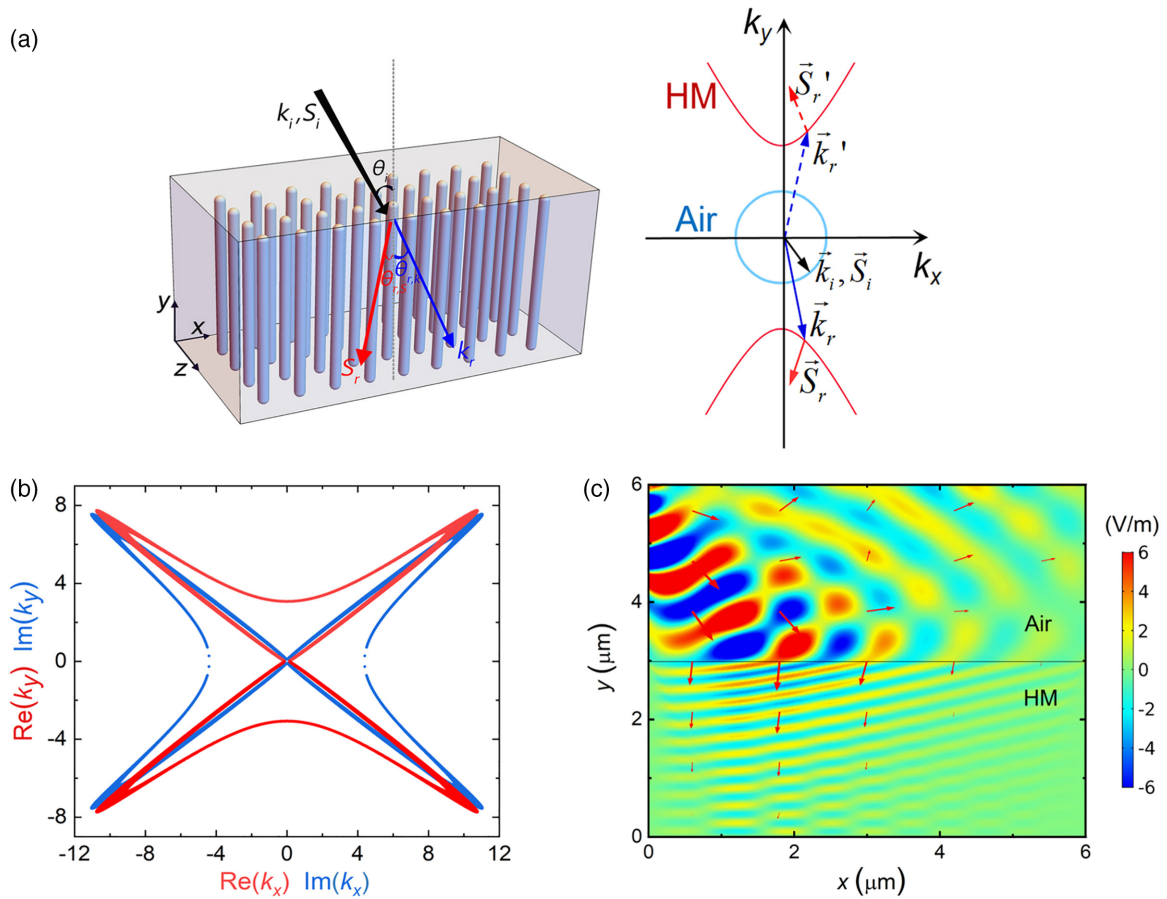


FIG. 4. Negative refraction in RuOCl₂. (a) Left: Schematic representation of negative refraction of a TM-polarized light incident from air to RuOCl₂. Right: The EFC projected onto the k_x - k_y plane. The refracted wave vectors and Poynting vectors are indicated by the solid blue and red arrows, respectively. The nonphysical solutions are represented by the dashed arrows. (b) Real part [Re(k)] and imaginary part [Im(k)] of wave vector in the wavelength of 911.7 nm. (c) The electric field distribution in the x - y plane for the TM light with the wavelength of 911.7 nm and an incident angle of 30°. The Poynting vectors are marked by red arrows.

y direction, $\omega_{p,y} = 7.02$ eV, enables $\text{Re} \varepsilon_y$ to cross zero at a higher energy of 3.36 eV. Furthermore, it is worth noting that the energy loss, as indicated by $\text{Im} \varepsilon$, is effectively suppressed within the hyperbolic window. This is attributed to the fact that the other bands, apart from the 1DEG band, are considerably distant from the Fermi level. As a result, only a few electron transitions occur at low energies, leading to the observed suppression of energy loss.

Doping is an effective strategy for manipulating the position of the 1DEG band relative to the Fermi level in RuOCl₂. By introducing electron doping, we investigated the dependence of the hyperbolic response window of RuOCl₂ on the Fermi energy (E_F) and the carrier concentration (n). When the electron doping concentration (n_e) increases from $6.6 \times 10^{20} \text{ cm}^{-3}$ to $6.6 \times 10^{21} \text{ cm}^{-3}$, the Fermi level is pushed upward by approximately 0.024–0.24 eV compared to pristine RuOCl₂. Although interband transitions are influenced by electron doping, which in turn affects the hyperbolic response of RuOCl₂, the overall hyperbolic interval experiences only a relatively small change less than 11.6% within the doping region. As shown in Fig. 3(c), at a doping concentration of $6.6 \times 10^{21} \text{ cm}^{-3}$, the upper limit of the hyperbolic window shifts from 3.35 to 2.96 eV. This implies that both

ν_F and $\omega_{p,y}$ are nearly unaffected by electron doping, as shown in Fig. 3(d), confirming the validity of the Q1DEG model. Based on these findings, it can be concluded that the long-wavelength plasmon frequency of RuOCl₂ follows the behavior expected in a Q1DEG system. Furthermore, the hyperbolic response window remains stable as the carrier concentration varies. It is worth noting that while the Q1DEG model is applicable to the systems with uniformly varying electron densities, it does not guarantee the same level of stability against localized environmental perturbations, such as defects. These perturbations could alter the linear energy-momentum dispersion relation or introduce additional energy states at the Fermi level, potentially impacting the stability of the hyperbolic response.

C. Hyperbolic response in RuOCl₂ crystal

The schematic diagram in Fig. 4(a) illustrates a beam of transverse magnetic (TM) polarized light incident on a RuOCl₂ crystal from air. The bulk RuOCl₂, with its Q1DEG nature, can be considered equivalent to an array of metallic nanorods. Aligned nanostructures, such as metallic nanorod arrays, have been instrumental in enhancing

optical properties and enabling the fabrication of nanoscale devices such as nanolasers [47], nanoresonators [48,49], and conductivity-enhanced photodetectors [50]. To simplify the analysis, we set the x axis as the optical axis parallel to the RuOCl₂/air interface, and the $x - y$ plane as the incident plane. According to the dispersion relation described in Eq. (2), when TM polarized light is incident from air ($\hat{\epsilon} = 1$) into a hyperbolic material ($\epsilon_{\perp} \equiv \epsilon_{yy} < 0$ and $\epsilon_{//} \equiv \epsilon_{xx} > 0$), the EFC of light dispersion transforms from a circle to a hyperbola. In the hyperbolic EFC, any real k_x value has a corresponding solution for k_y , indicating that hyperbolic materials can support wave propagation with extremely large wave vectors, as opposed to evanescent waves in free space. This forms the foundation for far-field imaging of subwavelength information using a hyperlens [51]. However, in practical hyperbolic materials, wave propagation cannot extend over an infinite range of wave vectors due to the presence of energy dissipation. In Fig. 4(b), we plotted the isofrequency k curves of bulk RuOCl₂, which comprise both the real part [Re(\mathbf{k})] and imaginary part [Im(\mathbf{k})] of the wave vector for TM electromagnetic waves at a wavelength of 911.7 nm, corresponding to a photon energy of 1.36 eV. Re(\mathbf{k}) represents the supported propagation modes, while Im(\mathbf{k}) represents the attenuation of these modes [52]. We observe that the propagation modes primarily occur along the y direction, while the damping modes predominantly occur along the x direction. The ideal hyperbola is truncated for very long wavelengths ($\lambda > \lambda_c$), indicating that when the wavelength exceeds λ_c , bulk RuOCl₂ behaves as a nonideal hyperbolic material.

Another intriguing optical phenomenon exhibited by hyperbolic materials is the all-angle negative refraction effect, which also stems from the extraordinary EFC. For the considered configuration in Fig. 4(a), negative refraction occurs at the interface (xz plane) between the hyperbolic media and the air, where both the electric field and the wave vector align within the xy plane. The time-averaged Poynting vector, which represents the directional energy flux of the electromagnetic wave, points to the direction normal to the EFC and is defined as [53]

$$\langle \mathbf{S} \rangle = \frac{1}{2} \mathbf{E} \times \mathbf{H}^* = \frac{\hat{\epsilon} \cdot \mathbf{k}}{2\omega\epsilon_0\epsilon_{//}\epsilon_{\perp}} H_0^2. \quad (9)$$

In the case of an incident TM wave propagating through an isotropic medium like air, \mathbf{S}_i is in the same direction as the incident wave vector \mathbf{k}_i . However, when the electromagnetic wave enters a hyperbolic medium, the direction of \mathbf{S}_r no longer aligns with the wave vector and instead lies on the same side of the interface normal as \mathbf{S}_i , indicating negative refraction, as depicted in Fig. 4(a), although there exist two solutions \mathbf{k}_r and \mathbf{k}_r^* for the refracted wave on both sides of k_x that satisfy the continuity of the tangential component of the wave vector. Only \mathbf{k}_r , following the causality principle and meeting the condition of $S_y > 0$, is physically meaningful [1]. The tangential component of the Poynting vector \mathbf{S} , which determine the nature of the refraction, is given by the expression

$$S_x = \frac{k_x}{2\omega\epsilon_0\epsilon_{\perp}} H_0^2. \quad (10)$$

Since $\epsilon_{\perp} < 0$ for the hyperbolic media and k_x exhibits continuity at the interface, the sign of S_x is reversed, leading to the phenomenon of negative refraction.

From the refraction angle determined by the Poynting vector,

$$\theta_{r,S} = \arctan\left(\frac{S_x}{S_y}\right) = \arctan\left(\frac{\sqrt{\epsilon_{//}} \sin \theta_i}{\epsilon_{\perp} \sqrt{1 - \sin^2 \theta_i / \epsilon_{\perp}}}\right), \quad (11)$$

we can deduce that negative refraction occurs in hyperbolic media for any incident angle θ . To demonstrate the negative refraction effect, we performed simulations when a transverse Gaussian beam is incident on bulk RuOCl₂, solving Maxwell's equations. The excitation wavelength was set to 911.7 nm, corresponding to a photon energy of 1.36 eV, at which $\epsilon_{xx} = 9.47 + 0.64i$ and $\epsilon_{yy} = -19.12 + 1.10i$. The incident angle of the Gaussian beam was set to 30°. The obtained electric field distribution and the variation of the directions of the Poynting vectors are presented in Fig. 4(c). Although the refraction waves can only propagate for a few wavelengths due to energy loss, the negative refraction effect is clearly observed.

Finally, we explore the propagation of the SPPs on the (001) surface of RuOCl₂ within the hyperbolic region. We adopted a RuOCl₂ sheet with a 0.5- μm radius and a 0.1- μm thickness, surrounded by air. Similar sizes have been used in the experimental study of surface hyperbolic polaritons [54,55]. These SPPs are excited by a vertically polarized dipole located just 1 nm above the RuOCl₂ surface. Specifically, at the frequency of $\hbar\omega = 1.36$ eV within the hyperbolic region, the permittivity tensor elements are $\epsilon_{xx} = 9.47 + 0.64i$, $\epsilon_{yy} = -19.12 + 1.10i$, and $\epsilon_{zz} = 7.78 + 0.62i$, respectively. By employing a finite-difference time-domain method for solving Maxwell's equations [40], we obtained the electric field distribution of the SPPs, as illustrated in Fig. 5. The energy of the SPPs is confined within narrow channels in the RuOCl₂ sheet, confirming the directional propagation features on the (001) surface, as depicted in Fig. 5(a). This directional propagation of SPPs can be attributed to the hyperbolic EFC of RuOCl₂. Notably, the electric field distributions in the x - z and y - z planes containing the dipole exhibit distinct features. In the x - z plane, as shown in Fig. 5(b), the SPPs do not exhibit significant anisotropic propagation behavior due to the close values of the real parts of ϵ_{xx} and ϵ_{zz} . However, in the y - z plane, as depicted in Fig. 5(c), the directional propagation of SPPs is clearly evident, aligning with the opposite signs of the real parts of ϵ_{yy} and ϵ_{zz} . This discrepancy in propagation behavior in different planes opens up a promising avenue for developing highly directional plasmonic waveguides and circuits, enabling the integration of complex optical functionalities into compact devices.

IV. CONCLUSIONS

In summary, we introduce the concept of a Q1DEGA mode for type-I NHMs. The inherent electronic anisotropy resulting from the unidirectional electron conduction nature gives rise to a type-I hyperbolic EFC and a wide hyperbolic response interval. Notably, the Q1DEGA mode exhibits an intriguing characteristic: the long-wavelength plasmon

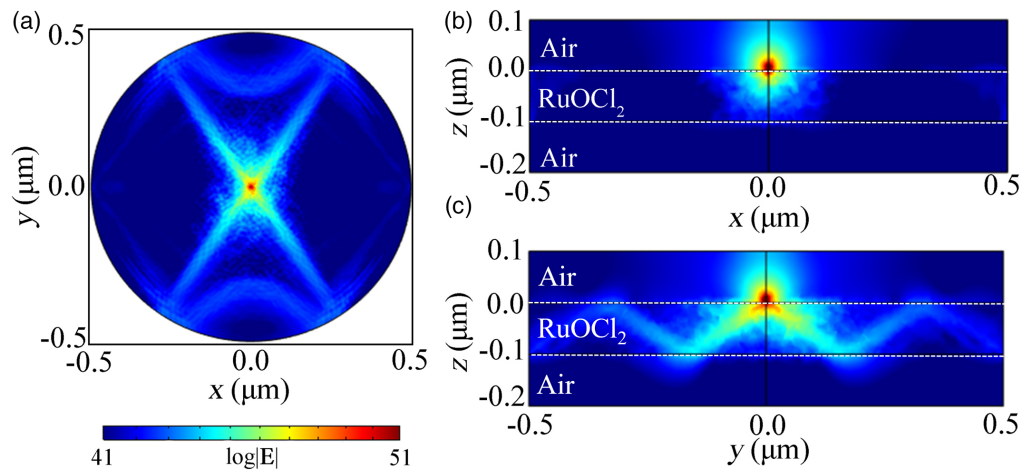


FIG. 5. The spatial distribution of electric field \mathbf{E} (log scale) of the SPPs at the frequency of $\hbar\omega = 1.36$ eV (wavelength of 911.7 nm) in the planes of (a) $z = 0$, (b) $y = 0$, and (c) $x = 0$. These SPPs are excited by a vertically polarized dipole located just 1 nm above the RuOCl_2 surface.

frequency, determining the negative permittivity component, shows an anomalous independence on carrier density (n). Our first-principles calculations identified a promising candidate material, RuOCl_2 , as an ideal type-I NHM, with a hyperbolic interval spanning from the infrared to the entire visible spectrum (369 nm–15.5 μm). Remarkably, the long-wavelength plasmon frequency and hyperbolic interval of RuOCl_2 remain resilient under variations in carrier density, aligning with the theoretical predictions of the Q1DEGA model. Additionally, the wave propagation behavior governed by the hyperbolic EFC displays an intriguing phenomenon of all-angle negative refraction and directional propagation of SPPs on the surfaces of RuOCl_2 . These findings underscore the potential of the Q1DEG model for designing NHMs. Notably, other materials

exhibiting similar crystal and electronic structures, such as OsOCl_2 , hold promise as well. We aim to inspire further theoretical research and experimental exploration into harnessing Q1DEGA systems for the development of innovative photonic or plasmonic devices.

ACKNOWLEDGMENTS

This study was supported by the National Natural Science Foundation of China (Grants No. 12074218 and No. 12304227), the Taishan Scholar Program of Shandong Province, and the Natural Science Foundation of Shandong Province (Grant No. ZR2023QA073).

- [1] D. R. Smith and D. Schurig, Electromagnetic wave propagation in media with indefinite permittivity and permeability tensors, *Phys. Rev. Lett.* **90**, 077405 (2003).
- [2] A. Aigner, J. M. Dawes, S. A. Maier, and H. Ren, Nanophotonics shines light on hyperbolic metamaterials, *Light-Sci. Appl.* **11**, 9 (2022).
- [3] H. Gao, L. Sun, and M. Zhao, Low-loss hyperbolic dispersion and anisotropic plasmonic excitation in nodal-line semimetallic yttrium nitride, *Opt. Express* **28**, 22076 (2020).
- [4] A. J. Sternbach, S. L. Moore, A. Rikhter, S. Zhang, R. Jing, Y. Shao, B. S. Y. Kim, S. Xu, S. Liu, J. H. Edgar, A. Rubio, C. Dean, J. Hone, M. M. Fogler, and D. N. Basov, Negative refraction in hyperbolic hetero-bicrystals, *Science* **379**, 555 (2023).
- [5] T. Zhang, C. Zheng, Z. N. Chen, and C.-W. Qiu, Negative reflection and negative refraction in biaxial van der Waals materials, *Nano Lett.* **22**, 5607 (2022).
- [6] Y. U. Lee, S. Li, G. B. M. Wisna, J. Zhao, Y. Zeng, A. R. Tao, and Z. Liu, Hyperbolic material enhanced scattering nanoscopy for label-free super-resolution imaging, *Nat. Commun.* **13**, 6631 (2022).
- [7] D. Lu, J. J. Kan, E. E. Fullerton, and Z. Liu, Enhancing spontaneous emission rates of molecules using nanopatterned multilayer hyperbolic metamaterials, *Nat. Nanotechnol.* **9**, 48 (2014).
- [8] G. I. López-Morales, M. Li, R. K. Yadav, H. R. Kalluru, J. K. Basu, C. A. Meriles, and V. M. Menon, Spontaneous emission dynamics of Eu^{3+} ions coupled to hyperbolic metamaterials, *Appl. Phys. Lett.* **118**, 011106 (2021).
- [9] Z. Guo, H. Jiang, and H. Chen, Hyperbolic metamaterials: From dispersion manipulation to applications, *J. Appl. Phys.* **127**, 071101 (2020).
- [10] D. Lee, S. So, G. Hu, M. Kim, T. Badloe, H. Cho, J. Kim, H. Kim, C.-W. Qiu, and J. Rho, Hyperbolic metamaterials: Fusing artificial structures to natural 2D materials, *Light* **2**, 1 (2022).
- [11] L. Y. Beliaev, O. Takayama, P. N. Melentiev, and A. V. Lavrinenko, Photoluminescence control by hyperbolic metamaterials and metasurfaces: A review, *Opto-Electron. Adv.* **4**, 210031 (2021).
- [12] S. Edalati-Boostan, C. Cocchi, and C. Draxl, MoTe_2 as a natural hyperbolic material across the visible and the ultraviolet region, *Phys. Rev. Mater.* **4**, 085202 (2020).
- [13] G. Ni, A. S. McLeod, Z. Sun, J. R. Matson, C. F. B. Lo, D. A. Rhodes, F. L. Ruta, S. L. Moore, R. A. Vitalone, R. Cusco,

- L. Artús, L. Xiong, C. R. Dean, J. C. Hone, A. J. Millis, M. M. Fogler, J. H. Edgar, J. D. Caldwell, and D. N. Basov, Long-lived phonon polaritons in hyperbolic materials, *Nano Lett.* **21**, 5767 (2021).
- [14] H. Gao, X. Zhang, W. Li, and M. Zhao, Tunable broadband hyperbolic light dispersion in metal diborides, *Opt. Express* **27**, 36911 (2019).
- [15] H. Gao, Z. Wang, X. Ma, X. Zhang, W. Li, and M. Zhao, Hyperbolic dispersion and negative refraction in a metal-organic framework Cu-BHT, *Phys. Rev. Mater.* **3**, 065206 (2019).
- [16] S. Hou, M. Wang, H. Gao, C. Ding, X. Zhang, L. Sun, X. Ma, Y. Li, and M. Zhao, Broadband hyperbolic plasmons in aluminum disulfide monolayer and its analogues: The role of orbital anisotropy, *Phys. Rev. B* **107**, 195410 (2023).
- [17] M. Wang, H. Gao, C. Ding, X. Zhang, S. Hou, L. Sun, X. Ma, Y. Li, and M. Zhao, Hyperbolic plasmons on natural biphenylene surface, *Carbon* **213**, 118307 (2023).
- [18] J. Sun, J. Zhou, B. Li, and F. Kang, Indefinite permittivity and negative refraction in natural material: Graphite, *Appl. Phys. Lett.* **98**, 101901 (2011).
- [19] M. N. Gjerding, R. Petersen, T. G. Pedersen, N. A. Mortensen, and K. S. Thygesen, Layered van der Waals crystals with hyperbolic light dispersion, *Nat. Commun.* **8**, 320 (2017).
- [20] K. Korzeb, M. Gajc, and D. A. Pawlak, Compendium of natural hyperbolic materials, *Opt. Express* **23**, 25406 (2015).
- [21] S. Das Sarma and E. H. Hwang, Collective modes of the massless Dirac plasma, *Phys. Rev. Lett.* **102**, 206412 (2009).
- [22] R. Sachdeva, A. Thakur, G. Vignale, and A. Agarwal, Plasmon modes of a massive Dirac plasma, and their superlattices, *Phys. Rev. B* **91**, 205426 (2015).
- [23] H. Gao, C. Ding, L. Sun, X. Ma, and M. Zhao, Robust broadband directional plasmons in a MoOCl₂ monolayer, *Phys. Rev. B* **104**, 205424 (2021).
- [24] C. Lian, S.-Q. Hu, J. Zhang, C. Cheng, Z. Yuan, S. Gao, and S. Meng, Integrated plasmonics: Broadband Dirac plasmons in borophene, *Phys. Rev. Lett.* **125**, 116802 (2020).
- [25] E. J. C. Dias, R. Yu, and F. J. García de Abajo, Thermal manipulation of plasmons in atomically thin films, *Light-Sci. Appl.* **9**, 87 (2020).
- [26] G. X. Ni, A. S. McLeod, Z. Sun, L. Wang, L. Xiong, K. W. Post, S. S. Sunku, B. Y. Jiang, J. Hone, C. R. Dean, M. M. Fogler, and D. N. Basov, Fundamental limits to graphene plasmonics, *Nature (London)* **557**, 530 (2018).
- [27] C. Ding, H. Gao, W. Geng, and M. Zhao, Anomalous plasmons in a two-dimensional Dirac nodal-line Lieb lattice, *Nanoscale Adv.* **3**, 1127 (2021).
- [28] J. Wang, X. Sui, W. Duan, F. Liu, and B. Huang, Density-independent plasmons for terahertz-stable topological metamaterials, *Proc. Natl. Acad. Sci. USA* **118**, e2023029118 (2021).
- [29] J. Wang, X. Sui, S. Gao, W. Duan, F. Liu, and B. Huang, Anomalous Dirac plasmons in 1D topological electrides, *Phys. Rev. Lett.* **123**, 206402 (2019).
- [30] W. Wu, Y. Liu, S. Li, C. Zhong, Z.-M. Yu, X.-L. Sheng, Y. X. Zhao, and S. A. Yang, Nodal surface semimetals: Theory and material realization, *Phys. Rev. B* **97**, 115125 (2018).
- [31] H. Hillebrecht, P. J. Schmidt, H. W. Rotter, G. Thiele, P. Zönnchen, H. Bengel, H. J. Cantow, S. N. Magonov, and M. H. Whangbo, Structural and scanning microscopy studies of layered compounds MCl₃ (M = Mo, Ru, Cr) and MOCl₂ (M = V, Nb, Mo, Ru, Os), *J. Alloy. Compd.* **246**, 70 (1997).
- [32] G. Kresse and J. Furthmüller, Efficient iterative schemes for *ab initio* total-energy calculations using a plane-wave basis set, *Phys. Rev. B* **54**, 11169 (1996).
- [33] P. E. Blöchl, Projector augmented-wave method, *Phys. Rev. B* **50**, 17953 (1994).
- [34] J. P. Perdew, K. Burke, and M. Ernzerhof, Generalized gradient approximation made simple, *Phys. Rev. Lett.* **77**, 3865 (1996).
- [35] S. Grimme, S. Ehrlich, and L. Goerigk, Effect of the damping function in dispersion corrected density functional theory, *J. Comput. Chem.* **32**, 1456 (2011).
- [36] V. I. Anisimov, F. Aryasetiawan, and A. I. Lichtenstein, First-principles calculations of the electronic structure and spectra of strongly correlated systems: The LDA+*U* method, *J. Phys.: Condens. Matter* **9**, 767 (1997).
- [37] W. Yang, L. Zhu, Y. Lu, E. Henriksen, and L. Yang, Point defects in two-dimensional RuCl₃, *Phys. Rev. Mater.* **7**, 064004 (2023).
- [38] Y. Tian, W. Gao, E. A. Henriksen, J. R. Chelikowsky, and L. Yang, Optically driven magnetic phase transition of monolayer RuCl₃, *Nano Lett.* **19**, 7673 (2019).
- [39] E. Şaşıoğlu, C. Friedrich, and S. Blügel, Effective Coulomb interaction in transition metals from constrained random-phase approximation, *Phys. Rev. B* **83**, 121101(R) (2011).
- [40] E. J. F. Dickinson, H. Ekström, and E. Fontes, COMSOL Multiphysics®: Finite element software for electrochemical analysis. A mini-review, *Electrochem. Commun.* **40**, 71 (2014).
- [41] S. Niu, G. Joe, H. Zhao, Y. Zhou, T. Orvis, H. Huyan, J. Salman, K. Mahalingam, B. Urwin, J. Wu, Y. Liu, T. E. Tiwald, S. B. Cronin, B. M. Howe, M. Mecklenburg, R. Haiges, D. J. Singh, H. Wang, M. A. Kats, and J. Ravichandran, Giant optical anisotropy in a quasi-one-dimensional crystal, *Nat. Photonics* **12**, 392 (2018).
- [42] M. Eldilo, F. Che, and M. Cada, in *Drude-Lorentz Model of Semiconductor Optical Plasmons* (Springer, New York), pp. 41–49.
- [43] See Supplemental Material at <http://link.aps.org/supplemental/10.1103/PhysRevB.109.115432> for the derivation of Eq. (6).
- [44] L. A. Falkovsky, Optical properties of graphene and IV–VI semiconductors, *Phys. Usp.* **51**, 887 (2008).
- [45] C. Hwang, D. A. Siegel, S. K. Mo, W. Regan, A. Ismach, Y. G. Zhang, A. Zettl, and A. Lanzara, Fermi velocity engineering in graphene by substrate modification, *Sci. Rep.* **2**, 590 (2012).
- [46] J. Singh, *Optical Properties of Condensed Matter and Applications* (John Wiley & Sons, New York, 2006), Vol. 6.
- [47] M. H. Huang, S. Mao, H. Feick, H. Yan, Y. Wu, H. Kind, E. Weber, R. Russo, and P. Yang, Room-temperature ultraviolet nanowire nanolasers, *Science* **292**, 1897 (2001).
- [48] Y. Sun, Y. Yin, B. T. Mayers, T. Herricks, and Y. Xia, Uniform silver nanowires synthesis by reducing AgNO₃ with ethylene glycol in the presence of seeds and (Vinyl Pyrrolidone), *Chem. Mater.* **14**, 4736 (2002).
- [49] S. Kar, B. N. Pal, S. Chaudhuri, and D. Chakravorty, One-dimensional ZnO nanostructure arrays: Synthesis and characterization, *J. Phys. Chem. B* **110**, 4605 (2006).

- [50] D. Zhang, C. Liu, B. Yin, R. Xu, J. Zhou, X. Zhang, and S. Ruan, Organics filled one-dimensional TiO₂ nanowires array ultraviolet detector with enhanced photo-conductivity and dark-resistivity, *Nanoscale* **9**, 9095 (2017).
- [51] Z. Liu, H. Lee, Y. Xiong, C. Sun, and X. Zhang, Far-field optical hyperlens magnifying sub-diffraction-limited objects, *Science* **315**, 1686 (2007).
- [52] R. M. Cordova-Castro, M. Casavola, M. van Schilfgaarde, A. V. Krasavin, M. A. Green, D. Richards, and A. V. Zayats, Anisotropic plasmonic CuS nanocrystals as a natural electronic material with hyperbolic optical dispersion, *ACS Nano* **13**, 6550 (2019).
- [53] Y. Liu, G. Bartal, and X. Zhang, All-angle negative refraction and imaging in a bulk medium made of metallic nanowires in the visible region, *Opt. Express* **16**, 15439 (2008).
- [54] Q. Zhang, Q. Ou, G. Hu, J. Liu, Z. Dai, M. S. Fuhrer, Q. Bao, and C.-W. Qiu, Hybridized hyperbolic surface phonon polaritons at α -MoO₃ and polar dielectric interfaces, *Nano Lett.* **21**, 3112 (2021).
- [55] C. Wang, S. Huang, Q. Xing, Y. Xie, C. Song, F. Wang, and H. Yan, Van der waals thin films of WTe₂ for natural hyperbolic plasmonic surfaces, *Nat. Commun.* **11**, 1158 (2020).